Tellus
SERIES B
CHEMICAL
AND PHYSICAL
METEOROLOGY
PUBLISHED BY THE INTERNATIONAL METEOROLOGICAL INSTITUTE IN STOCKHOLM

Tellus (2009), 61B, 131–143
Printed in Singapore. All rights reserved

TELLUS

Spatial distribution and optical properties of Saharan dust observed by airborne high spectral resolution lidar during SAMUM 2006

By MICHAEL ESSELBORN[1]*, MARTIN WIRTH[1], ANDREAS FIX[1], BERNADETT WEINZIERL[1], KATHARINA RASP[1], MATTHIAS TESCHE[2] and ANDREAS PETZOLD[1],
[1]*Institut für Physik der Atmosphäre, Deutsches Zentrum für Luft– und Raumfahrt (DLR), Oberpfaffenhofen, 82234 Wessling, Germany;* [2]*Leibniz–Institut für Troposphärenforschung (IFT), 04318 Leipzig, Germany*

(Manuscript received 31 December 2007, in final form 22 July 2008)

ABSTRACT

Airborne measurements of pure Saharan dust extinction and backscatter coefficients, the corresponding lidar ratio and the aerosol optical thickness (AOT) have been performed during the Saharan Mineral Dust Experiment 2006, with a high spectral resolution lidar. Dust layers were found to range from ground up to 4–6 km above sea level (asl). Maximum AOT values at 532 nm, encountered within these layers during the DLR Falcon research flights were 0.50–0.55. A significant horizontal variability of the AOT south of the High Atlas mountain range was observed even in cases of a well-mixed dust layer. High vertical variations of the dust lidar ratio of 38–50 sr were observed in cases of stratified dust layers. The variability of the lidar ratio was attributed to dust advection from different source regions. The aerosol depolarization ratio was about 30% at 532 nm during all measurements and showed only marginal vertical variations.

1. Introduction

Mineral dust is one of the major constituents of the atmospheric aerosol and strongly contributes to the global aerosol optical thickness (AOT; Tegen et al., 1997; Haywood et al., 2001). The estimation of the radiative forcing effects of mineral dust is considerable but still highly uncertain (Solomon et al., 2007). Difficulties in quantifying radiative effects are primarily due to the distinct variability of the dust spatial and temporal distribution and uncertainties associated with dust optical properties. To improve the understanding of the mineral dust radiative effects, the Saharan Mineral Dust Experiment (SAMUM), funded by the German Research Foundation (DFG), was carried out during May/June 2006 in Morocco, to characterize the optical, chemical and microphysical properties of pure mineral dust close to the Saharan desert, its major source region (Heintzenberg, 2008).

Key parameters for determining the climatic impact of aerosols like mineral dust are their extinction coefficients, as well as the their spatial distribution (Haywood and Boucher, 2000; Penner et al., 2001). Light detection and ranging (lidar) instruments are particularly suitable for remote sounding of the atmospheric aerosol because of their high spatial and temporal resolution. In contrast to a conventional backscatter lidar, a high spectral resolution lidar (HSRL) is designed to spectrally separate the narrow band-width aerosol return from the strongly Doppler-broadened molecular backscatter spectrum (Shimizu et al., 1983; Shipley et al., 1983; Piironen and Eloranta, 1994). The decrease of molecular backscatter is used likewise in the Raman lidar technique (Ansmann et al., 1990) to directly determine aerosol extinction. Thus, no assumptions about the extinction-to-backscatter ratio, the so-called lidar ratio, are required. The latter is a prerequisite for retrieving extinction profiles from a conventional backscatter lidar and needs to be estimated. However, the strong dependence of the lidar ratio on the aerosol's physical properties results in large uncertainties in the extinction retrieval of normal backscatter lidars. Thus, HSRL measurements provide useful information for conventional backscatter lidars like the Cloud-Aerosol LIdar with Orthogonal Polarization (CALIOP) instrument aboard the Cloud-Aerosol Lidar and Infrared Pathfinder Satellite Observation (CALIPSO) satellite (Winker et al., 2007). Airborne HSRL measurements are particularly useful because they can be coordinated for validation purposes and allow nearly real-time spatial overlap along the satellite foot print.

So far, a few lidar ratio measurements have been reported for Saharan dust. However, these measurements were restricted

*Corresponding author.
e-mail: Michael.Esselborn@dlr.de
DOI: 10.1111/j.1600-0889.2008.00394.x

to cases of long-range transport of dust and did not refer to measurements very close or over the dust source region. Cases of dust transport to southern Europe (De Tomasi et al., 2003; Amiridis et al., 2005; Mona et al., 2006), central Europe (Mattis et al., 2002; Müller et al., 2003), the Canary Islands (Powell et al., 2000; Welton et al., 2000) and the North Atlantic region (Voss et al., 2001) have been observed. Very recently, Papayannis et al. (2008) presented the first coordinated dust lidar ratio measurements over the whole European continent, performed in the frame of the EARLINET project (Bösenberg et al., 2003). However, mixing with anthropogenic pollution or maritime aerosols during long-range transport is found to significantly influence the lidar ratio (Papayannis et al., 2005, 2008).

As part of SAMUM, the vertical structure and horizontal extend of Saharan dust plumes as well as their optical properties were measured by airborne HSRL between the Atlantic coast in the northwest of Morocco and the Algerian boarder in the southeast. Because of the vicinity to the dust source regions and the low population density, pure Saharan dust could be observed by HSRL for the first time to the best of our knowledge.

The purpose of this paper is a detailed description of the dust plumes' spatial distribution close to their source regions and a characterization of the pure Saharan dust in terms of its lidar ratio and depolarization ratio. Moreover, the horizontal variability of the AOT encountered on the DLR Falcon research flights is discussed in detail.

2. Experimental methods

2.1. Airborne high spectral resolution lidar

The airborne HSRL applied during SAMUM is based on a high-power, injection-seeded, frequency-doubled Nd:YAG laser transmitter and an iodine absorption cell. The system is designed to measure atmospheric backscatter and linear depolarization at 1064 and 532 nm as well as molecular backscatter at 532 nm. A detailed description of the HSRL system, its data products and an assessment of its measurement accuracy can be found in (Esselborn et al., 2008). The laser transmitter consists of a diode pumped, *Q*-switched Nd:YAG oscillator with injection seeding and three successive power amplifiers. The system is frequency stabilized to an iodine absorption line and operated at 100 Hz. For the HSRL measurements the fundamental radiation is frequency doubled to yield a pulse energy of 100 mJ at 532 nm. Both wavelengths are transmitted in a coaxial mode into the atmosphere. The backscattered light is collected by means of a Cassegrain telescope with an aperture diameter of 35 cm. A fieldstop located in the focal plane of the telescope limits the acceptance angle to 1 mrad. A schematic of the receiver module used for the detection of the lidar signals is shown in Fig. 1. A dichroic beamsplitter is used to spectrally separate the backscatter signals at 1064 and 532 nm. An iodine vapour cell within the molecular channel at 532 nm suppresses the aerosol backscatter, so that AOT profiles as well as extinction and backscatter coefficients can be derived directly from the attenuated molecular backscatter. For polarization sensitive detection the receiver module is equipped with a cross-polarized channel at the two wavelengths, respectively. The atmospheric backscatter is detected with avalanche photodiodes (APDs) in case of 1064 nm and with photomultipliers (PMTs) at 532 nm. Vertical resolution of the measured profiles is 15 m for all backscatter and depolarization raw data. Because the aerosol extinction coefficient is derived from the measured AOT profile by numerical differentiation, vertical resolution is decreased (360–700 m) in cases of extinction and lidar ratio profiles, to reduce the statistical error. Relative systematic errors of the backscatter measurements are typically 4% to 8% within the dust layers and statistical errors are negligible (Esselborn et al., 2008). In case of the extinction measurements, relative systematic errors are usually less than 5%, so that statistical errors of typically 5% to 20% are dominant. Relative systematic errors of the depolarization measurements are primarily due to mechanical accuracy of the calibration measurement and results in a relative error of the aerosol depolarization ratio of the order of 10% to 16% (see also Esselborn et al., 2008). The HSRL system specifications are listed in Table 1.

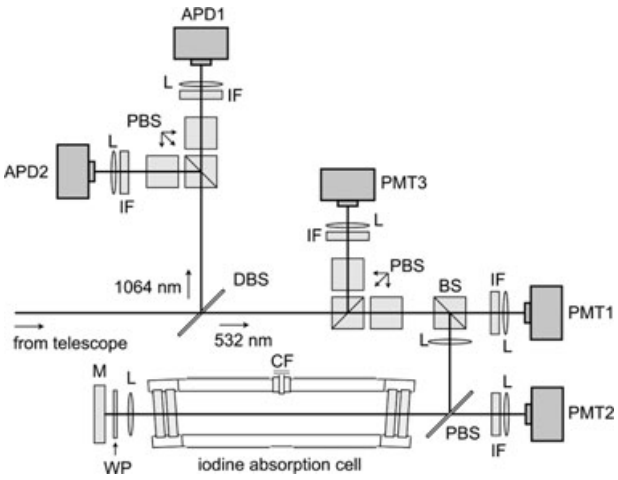

Fig. 1. Schematic of the receiver module used for detection at 532 and 1064 nm. APD: avalanche photo diode, BS: beam splitter, CF: cool finger, DBS: dichroic beam splitter, IF: interference filter, L: lens, M: mirror, PBS: polarization beam splitter, PMT: photomultiplier, WP: quarter wave plate.

2.2. Falcon flight missions during SAMUM 2006

During the SAMUM field phase the HSRL was operated aboard the DLR Falcon aircraft, which was based on Casablanca Mohamed V International Airport (33.59°N, 7.61°W, 15 m asl; CMN hereafter). From there, a total of eight research flights

Table 1. System parameters of the HSRL system

Transmitter	
Pulse energy at 1064 nm	220 mJ
Repetition rate	100 Hz
Pulse energy at 532 nm	100 mJ
Frequency fluctuations at 532 nm	<5 MHz
Spectral purity at 532 nm	99.96%
Laser band-width at 532 nm	<90 MHz
Receiver	
Telescope diameter	350 mm
Iodine absorption band-width	2 GHz
Optical iodine filter length	380 mm
Detector's field of view	1 mrad
Detector's analoge to digital conversion resolution	14 bit
Detector's sampling rate	10 MHz

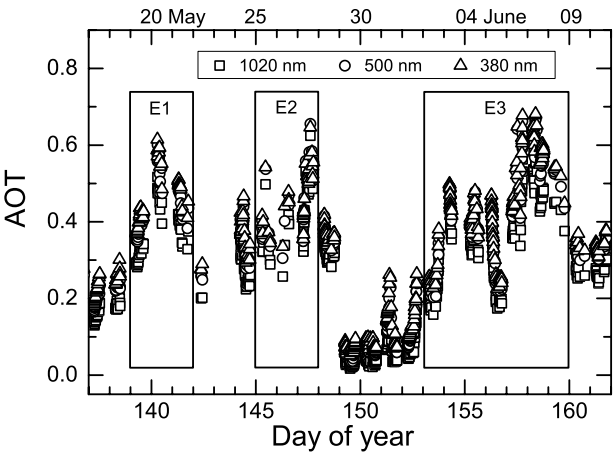

Fig. 2. Time-series of AOT measured at OZZ between 17 May and 11 June with a Sun photometer at 1020, 500 and 380 nm. The rectangles indicate the duration of the respective dust episodes.

were performed. Most of the local flight strategies during SAMUM involved two sections: first, remote sounding of the atmosphere over the ground stations in Ouarzazate (30.93°N, 6.90°W, 1133 m asl; OZZ hereafter) and Tinfou, located 30 km southeast of Zagora (30.34°N, 5.84°W, 726 m asl; ZAG hereafter) at high flight altitude with HSRL to measure the overall atmospheric extinction profile. Second, performing flight legs at altitudes where dust layers have been detected by lidar before to conduct in situ measurements. The in situ instrumentation included various aerosol sensors measuring the particle size distribution from 4 nm to 100 μm and a three-wavelength aerosol absorption photometer (Petzold et al., 2008; Weinzierl et al., 2008). Volatility studies were conducted using a novel instrument configuration consisting of condensation particle counters (CPC), which were partially equipped with diffusion screen separators. Thus, a comprehensive set of information of the atmospheric column has been achieved.

To compare the novel airborne HSRL with the ground based lidars, ground based measurements and flight activities were coordinated. During SAMUM, three depolarization sensitive Raman lidars were deployed at OZZ ground station. Instrument comparisons and statistics of the aerosol's properties measured by Raman lidar are discussed by Tesche et al. (2008). Using the ensemble of lidars deployed during SAMUM coincident measurements of the desert dust depolarization ratio at four wavelengths (355, 532, 710 and 1064 nm) were made for the first time to the best of our knowledge. The detailed analysis of the coordinated depolarization measurements are presented by Freudenthaler et al. (2008). For a short period, the POLIS Raman lidar was moved from OZZ to ZAG to support the ground based measurements with vertically resolved extinction and backscatter profiling. For instrument intercomparison, the airborne HSRL measurements over this ground station were coordinated as well. Moreover, the Falcon flight missions were coordinated with satellite overpasses of the Multi-angle Imaging SpectroRadiometer (MISR) and the Medium Resolution Imaging Spectrometer (MERIS; Dinter et al., 2008) for validation purposes. A comparison of the AOT measurements obtained by MISR and HSRL can be found in Kahn et al. (2008).

Figure 2 shows a time-series of AOT values measured at three different wavelengths by a Sun photometer at OZZ ground station during 17 May and 11 June 2006. As can be seen, three dust events with a maximum AOT higher than 0.6 at 500 nm are separated by clean air intervals. This time-series is used to separate the period of the Falcon deployment during the SAMUM field phase into three episodes ranging from 19 to 22 May (Episode 1), 25 to 28 May (Episode 2) and 2 to 9 June 2006 (Episode 3). During all dust episodes Falcon flight missions were conducted.

An overview of the Falcon research flights (RF) is given in Table 2. Here we focus on the analysis of six local research flights, whose flight tracks are shown in Fig. 3. One research flight (RF 4, 28 May) was dedicated to study long-range transport of Saharan dust and was routed towards Portugal. The results of this flight are presented by Wagner et al. (2008).

3. Results

3.1. Case study of marine air intrusion on 3 June 2006

The first part of flight mission RF6 (cf. Fig. 3d) was dedicated to study the spatial dust distribution between the Moroccan mainland and the Atlantic coast. After takeoff at CMN at 01:30 UTC the DLR Falcon first headed northwards over the Atlantic Ocean during climb flight, than turned southwards to overfly the Atlantic coast and the High Atlas mountain range at a flight altitude of 10.5 km asl. Over OZZ the Flacon turned southeast to overfly ZAG and then started descending to perform in situ measurements. Figure 4 shows the cross-section of the

Table 2. Flight missions of the DLR Falcon during SAMUM Field Campaign 2006

Episode	Date	Research Flight	Routing	Takeoff–Landing (UTC)
E1	19 May	RF1	CMN–OZZ	10:33–12:12
	20 May	RF2	CMN–OZZ–ZAG–CMN	10:34–13:48
	22 May	RF3	OZZ–ZAG–OZZ	16:17–18:15
LRT	27 May	RF4	CMN–Cabo da Roca–Evora–CMN	09:15–12:36
E2	28 May	RF5	CMN–OZZ–ZAG–CMN	10:12–13:35
E3	3 June	RF6	CMN–OZZ–ZAG–CMN	01:30–04:45
	3 June	RF7	CMN–OZZ–ZAG–OZZ	07:13–09:08
	4 June	RF8	CMN–OZZ–ZAG–CMN	09:15–12:35

CMN, Casablanca Mohamed V International Airport, OZZ, Ouarzazate Airport, ZAG, Zagora, LRT, Long-range transport

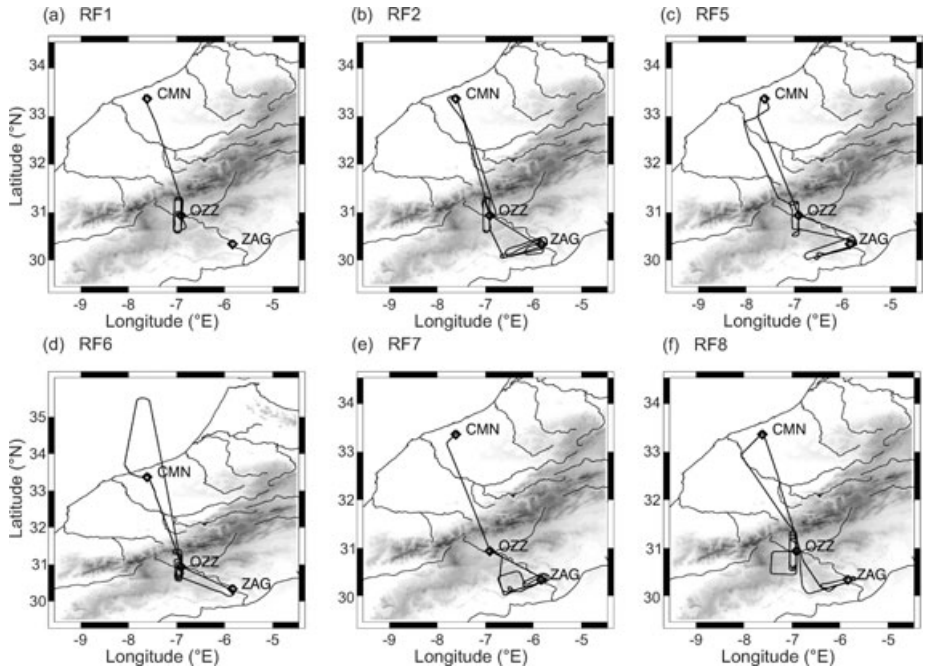

Fig. 3. Falcon flight tracks on 19 May (a), 20 May (b), 28 May (c), 3 June, night (d), 3 June (e) and 4 June (f).

measured backscatter ratio during 02:08–02:52 UTC. The cross-section spreads over more than 600 km from north to south. Cirrus clouds can be seen at an altitude of 6–10 km asl. The dust layer south of the High Atlas mountain range is vertically split in two parts with backscatter ratio values of up to 6 within the lower layer and less than 3 within the upper one. The top layer height is clearly defined at 4.5 km asl. During this flight leg, a distinct land–sea–wind circulation could be observed extending about 300 km from the Atlantic coast up to the Atlas mountains. In order to illustrate the land-sea-wind circulation, isolines of the meridional component of the horizontal wind vector have been overlaid. Solid lines correspond to positive values of the meridional component and indicate advection towards northerly directions. In contrast, dashed lines with negative values indicate southerly advection. The wind field is based on the 6-hourly operational analyses of the ECMWF (European Centre for Medium-Range Weather Forecast) and has been interpolated in space and time to the Falcon flight track. As it can be seen, air masses at altitudes below 3 km asl are advected from over the Atlantic Ocean towards the Atlas mountain. Within the layer between 3–5 km asl the meridional wind orientation is reversed. The zonal component (not shown) is small compared with the meridional component and turns from easterly advection within the layer below 3 km asl to westerly advection within the layers above. By means of this circulation, a lofted Saharan dust plume is transported towards northern directions at an altitude of $\approx$4 km asl. For representation of topography GLOBE elevation data (GLOBE Task Team and others, 1999) have been used.

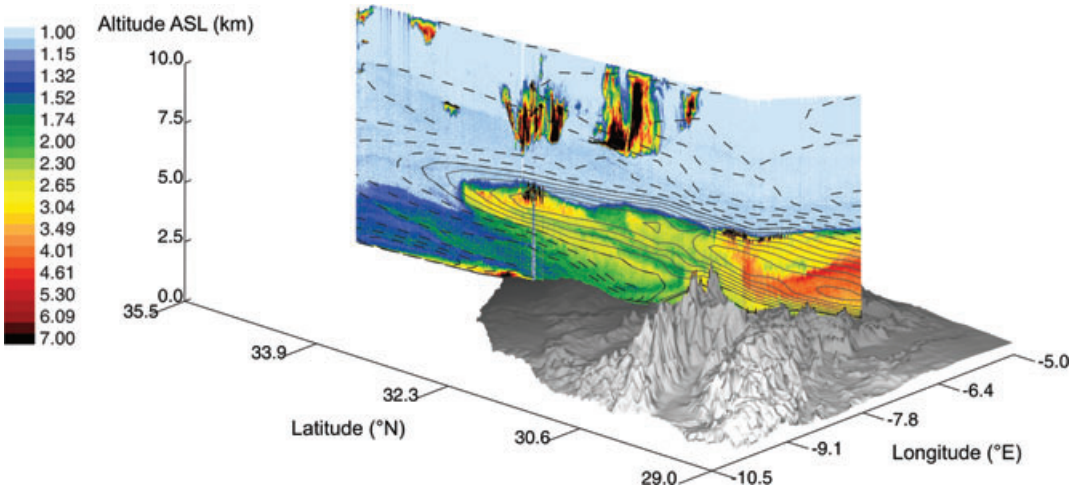

Fig. 4. Backscatter ratio measured during RF6 from 02:08–02:52 UTC. The cross-section extends over approximately 600 km from the Atlantic Ocean over the High Atlas mountain range towards the southern part of Morocco. The contours indicate advection towards northerly (solid lines) and southerly (dashed lines) directions, respectively. For representation of topography GLOBE elevation data have been used.

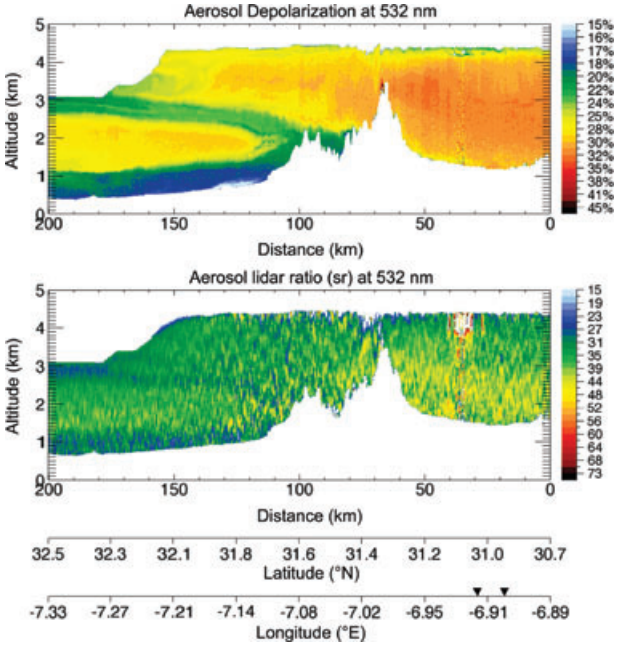

Fig. 5. Aerosol depolarization and lidar ratio measurement during RF6. The influence of maritime air masses north of the Atlas mountains result in a decrease of both aerosol quantities.

Figure 5 shows a detail of the aerosol depolarization and the lidar ratio measurement during the descent towards CMN on the same flight during 04:12–04:29 UTC (the flight direction was northbound on the way back, thus the distance axis is reversed). During the descent, the aircraft was within the dust layer in between a distance of 150–200 km. As it can be identified by the spatial variation of aerosol depolarization and lidar ratio the land-sea-wind circulation persisted to the time of descent. The aerosol depolarization ratio shows values of ≈30% within the dust layers south of the Atlas mountains. In contrast, aerosol depolarization is drastically decreased (17%–23%) within the airmass advected from the Atlantic Ocean. The relatively small values of aerosol depolarization can be attributed to the influence of maritime aerosol (Sakai et al., 1999). The lidar ratio measurement north of the Atlas mountains indicates the Atlantic air intrusion with relatively small lidar ratios of 25–30 sr, which are typical for sea salt particles (Ansmann et al., 2001; Papayannis et al., 2005; Mona et al., 2006). Unlike the almost height independent aerosol depolarization, the lidar ratio exhibits a slight two-layer structure south of the Atlas mountains. The values range from 41 sr within the upper layer to 47 sr within the lower one. Because of the dust advection from southern directions, the effective blocking of the marine intrusion by the Atlas mountains and the low population density within the southern part of Morocco, this vertical variation is unlikely to arise from mixing with other aerosol types. As a potential explanation of the lidar ratio variation within pure dust layers, dust advection from different regions will be discussed at a later stage of this paper. In the following we concentrate on the characteristics of pure Saharan dust observed in the southern part of Morocco.

3.2. *Spatial distribution of Saharan dust plumes*

The dust layers probed during the Falcon research flights between the High Atlas mountain range and the Algerian border extended from ground up to 4–6 km asl. Besides well-mixed layers, a complex internal structure during the development of the boundary layer or the advection of dust plumes could be observed several times. Figures 6a and b show the lidar observations of the research flights RF1 and RF2 conducted during Episode 1. Both diagrams show the cross-sections measured

during the long north-south flight legs of the flight patterns depicted in Figs. 3a and b. The measurements were made on 19 May during 10:50–11:10 UTC and on 20 May during 10:50–11:16 UTC, respectively. The arrows on the longitude/latitude axis mark changes in the flight direction. The summits of the Atlas mountains reach about 3 km asl. North of the Atlas mountain range the measured cross-section of RF1 shows a very well mixed dust layer with a sharply defined boundary at a constant height of 5.5 km above sea level (asl). South of the Atlas the boundary is on average 0.5 km lower and exhibits some degree of wavelike modulation, which is attributed to small scale convection. The backscatter ratio shows virtually no variation north of the Atlas and only little changes within the southern part of the cross-section. Here, the backscatter ratio is about 2.5 within the lower dust layer underneath 3 km asl. Slightly higher values around 2.9 can be found within the upper dust layer. The measured cross-section of RF2 indicates a dust layer boundary at 6 km asl. Several convective clouds spread at the top of the dust layer above the Atlas mountains and at the southern part of the cross-section. Detached dust filaments can be identified above the dust boundary. As in the case of RF1 the dust layer appears more homogeneous north of the Atlas mountains. Compared with RF1, the two-layer structure south of the Atlas is more pronounced on RF2.

During research flight RF5 (Fig. 6c), distinct horizontal and vertical variations in the dust loading were observed. The measurements were made at the same time of day like those of Episode 1. A rather well mixed dust layer above the southern Atlas foothills and a two-layer structure at the southern part of the cross-section can be identified. The upper dust layer boundary is at 4 km asl. The lower dust layer boundary ranges from 2–2.5 km asl.

Research flights RF6, RF7, and RF8 (Figs. 6d–f) were made during Episode 3. The data of Fig. 6d where measured on a north-south flight leg shortly after the one shown in Fig. 4. All cross-sections exhibit distinct horizontal and vertical variability. The measurements of RF7 were made approximately 4 h later than those of the night flight RF6. Thus, the two-layer structure south of the Atlas mountains can be seen in both Figs. 6d and e with a higher dust loading within the lower layer (note the different scale of the horizontal axis). The backscatter ratio cross-section of RF8 (Fig. 6f) exhibits a complex vertical stratification and an increasing dust loading towards the south of the cross-section. Dust layer boundaries ranged from 4to 4.5 km asl as measured during this episode.

3.3. Horizontal variability of the AOT

The AOT data were derived from the measured AOT profiles between flight altitude and ground surface by averaging the last thre range bins above ground. Since the vertical resolution of the AOT profiles is 15 m, the AOT data are the average over 45 m above ground. Horizontally the AOT values were smoothed using a moving average to reduce noise. The lateral resolution and the number of averaged values, respectively, was chosen such that the relative statistical error is of the order of 5%–10%. The AOT along the Falcon flight track is shown for the 3 d (19 May, 28 May and 4 June) of the MISR overpasses. Figure 7a shows the measured AOT during RF1 from 10:50 to 11:13 UTC along a flight distance of approximately 300 km. The horizontal resolution is 2.9 km and corresponds to the horizontal extension of the average. North of the Atlas mountains (Latitude $> 31.5^{\circ}$), the AOT values are relatively high and average out at 0.43. The variation south of the Atlas is more pronounced with values ranging from 0.25–0.45. The AOT measured during RF5 from 10:35 to 11:15 UTC (Fig. 7b) shows lower values ranging from 0.25 to 0.37 with less variability. The horizontal resolution is 8.3 km. The covered distance of this flight leg is 440 km. Figure 7c shows the AOT measured along the Falcon flight track during RF8 between 10:46 and 11:25 UTC with a horizontal resolution of 3.2 km. The covered distance of this flight leg is 420 km. Strong horizontal variations of the AOT ranging from 0.2 to 0.5 were observed. Positions at which clouds were detected have been blanked out.

Direct determination of the AOT, together with precise observation of the dust layer thickness by means of HSRL, allows to investigate the horizontal variability of the AOT. The influence of topography and inhomogeneities of dust plumes on the amount of AOT can be studied separately. To identify the cause of the significant regional AOT variations encountered on 19 May and 4 June, the measured AOT along the Falcon flight path has been divided by the dust layer thickness such that an average AOT per unit length is obtained. In the following this is referred to as 'AOT related to layer thickness'. Because the dust layers usually extended from ground up to a sharply defined boundary (cf. Fig. 6), the dust layer thickness could be determined accurately.

Figure 8a shows the AOT (upper curve) as function of flight distance on RF1 during the same period as shown in Fig. 7a. The statistical error bounds of the AOT measurement are shaded. For validation purpose, the result of the coincident Sun photometer measurement at 500 nm made at OZZ ground station is included. Considering the different measurement ranges and geometries of the airborne HSRL and the groundbased Sun photometer, the AOT measurements of both instruments agree very well. The influence of the Atlas mountains' topography becomes clearly visible with the drastic decrease of AOT values right above the Atlas' summits (at distance of $\approx$100 km). The AOT related to layer thickness is shown as the lower curve and amounts to $(0.08 \pm 0.007)\,\mathrm{km}^{-1}$. The little variation of the AOT related to layer thickness indicates well mixed layer. In this homogeneous case, the layer thickness related AOT is equal to an average aerosol extinction coefficient.

Figure 8b shows the AOT (upper curve) as function of flight distance on RF8. Sun photometer and HSRL measurements

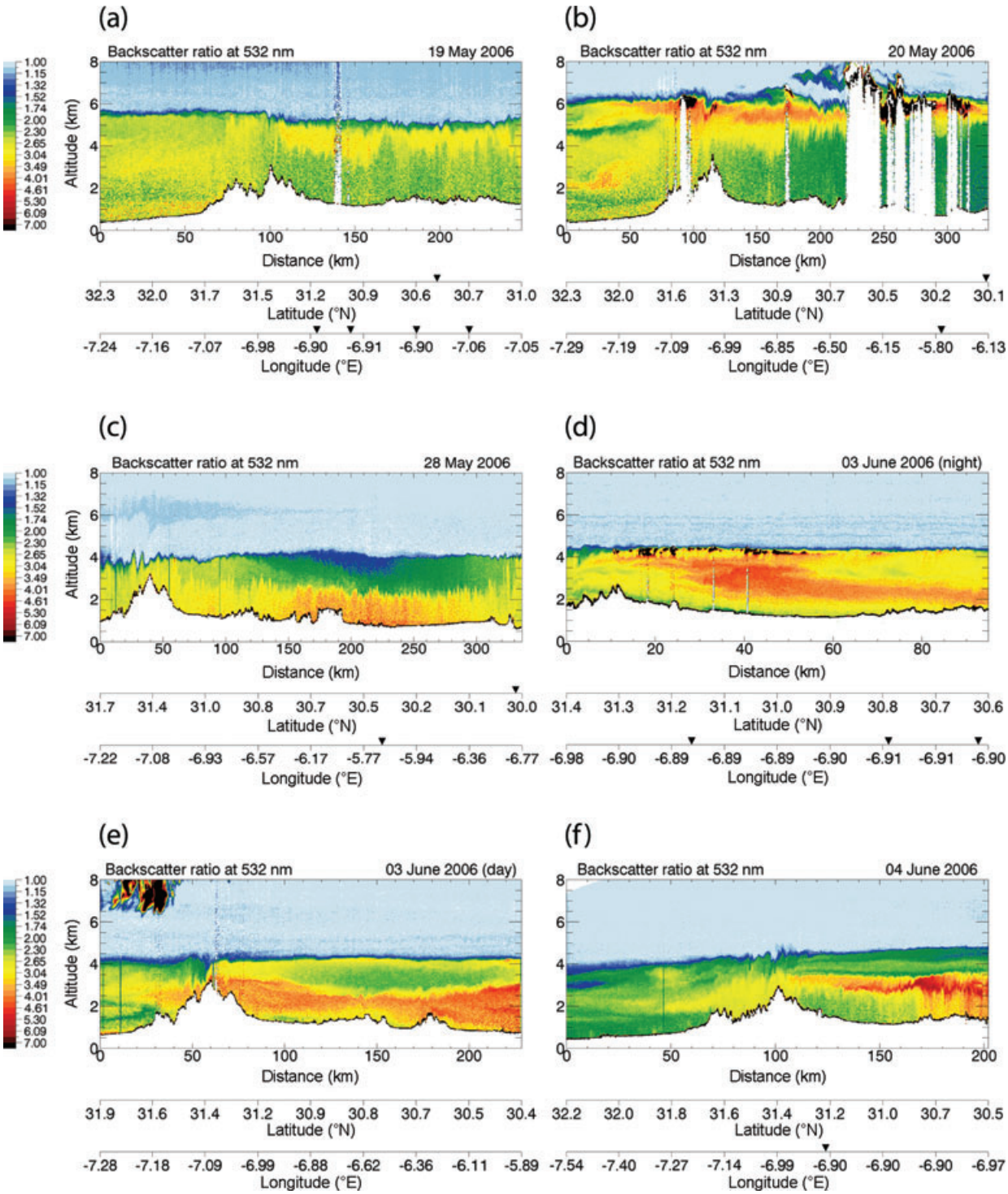

Fig. 6. Backscatter ratio cross-sections measured on 19 May from 10:50–11:10 UTC (a), 20 May from 10:50–11:16 UTC (b), 28 May from 10:35–11:05 UTC (c), 3 June from 03:12–03:20 UTC (d), 3 June from 07:25–07:42 UTC (e) and 4 June 09:35–09:51 UTC (f). Arrows on the longitude/latitude axis indicate changes in the flight direction of the aircraft.

are in good agreement in this case as well. The AOT related to layer thickness is shown as the lower curve and averages out to 0.09 km^{-1} with a relatively large standard deviation of $\pm 0.02\ km^{-1}$. In this case the variability of the AOT is not only due to the influence of topography but is attributed to advection of dust plumes (cf. Fig. 6f). The resolved AOT peaks in this figure are ascribed to an inhomogeneous stratification of the advected dust plume.

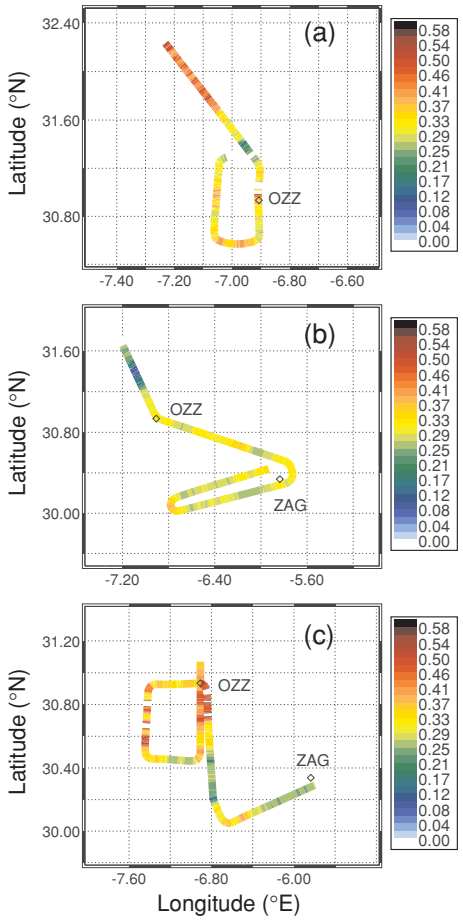

Fig. 7. AOT measured along the Falcon flight track on 19 May from 10:50–11:13 UTC with horizontal resolution of 2.9 km (a), 28 May from 10:35–11:15 UTC with horizontal resolution of 8.3 km (b) and 4 June from 10:46 to 11:25 UTC with horizontal resolution of 3.2 km (c).

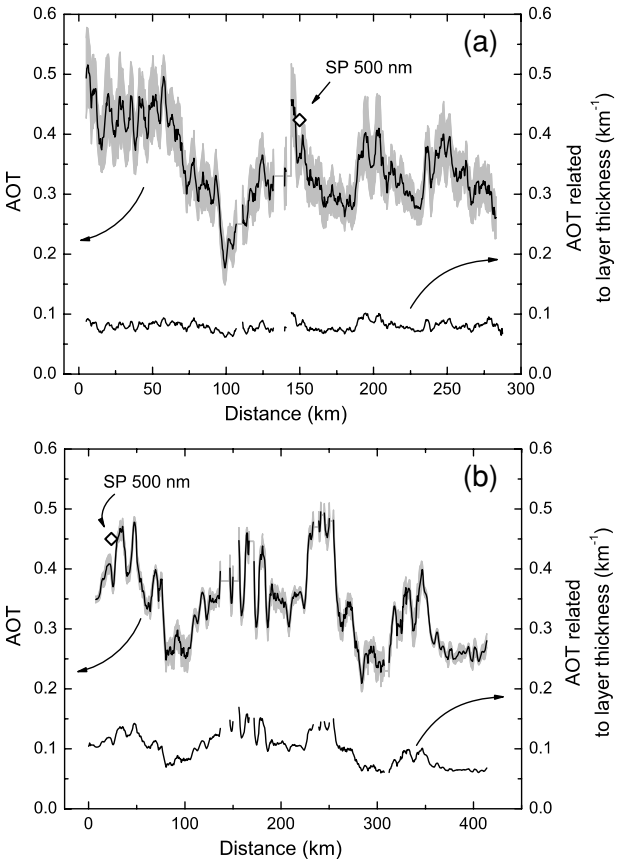

Fig. 8. (a) AOT measurement by airborne HSRL at 532 nm along the Falcon flight track on 19 May 2006 from 10:50 to 11:13 UTC. The diamond denotes the Sun photometer measurement at OZZ at 10:55 UTC. The lower curve shows the AOT related to the dust layer thickness. The shaded area denotes the statistical error of the measurement. (b) AOT measurement on 4 June from 10:46 to 11:25 UTC. The Sun photometer measurement at OZZ was at 10:41 UTC.

3.4. *Vertical profiling of the lidar ratio and aerosol depolarization*

Figure 9 shows column averaged HSRL lidar ratio measurements (filled squares) during six Falcon flights over OZZ compared to the time-series of lidar ratio measurements conducted at OZZ ground station by the IFT. The receiver of the IFT Raman lidar (Backscatter Extinction lidar-Ratio Temperature Humidity Profiling Apparatus, BERTHA) provides 14 channels altogether to detect atmospheric backscatter separated in elastic, vibrational, and rotational Raman shifted and depolarized backscatter (Tesche et al., 2008). The column averaged rotational (532 nm) and vibrational (355 and 532 nm) Raman lidar measurements indicate a variation of the lidar ratio in the range of 40–60 sr during the period from 12 May to 6 June. Apart from 28 May where no direct comparison with Raman lidar measurements was possible, the results of both independent instruments agree very well.

Depending on the vertical structure of the dust layers, the lidar ratio shows variations along the profile which are significant regarding the measurements' error bounds. Figure 10 shows averaged profiles of aerosol backscatter (Fig. 10a) and extinction (Fig. 10b) coefficients as well as the vertical structure of the aerosol lidar ratio (Fig. 10c) and depolarization ratio (Fig. 10d) measured during RF1. The profiles were averaged close to OZZ ground station over a period of 284 s. The error bars denote the 3-*sigma* statistical error, the systematic error bounds are shaded. The wind direction profile (Fig. 10e) as measured with the Falcon standard meteorological equipment during a descent to OZZ indicates turbulence from surface up to 5 km asl and a defined westerly advection at higher altitudes. The potential temperature is almost constant with height ($\Theta = 315$ K) within the dust layer and shows a pronounced inversion at the boundary indicating a well mixed dust layer from surface to an altitude of 5 km asl. As expected, both backscatter and extinction profiles are very

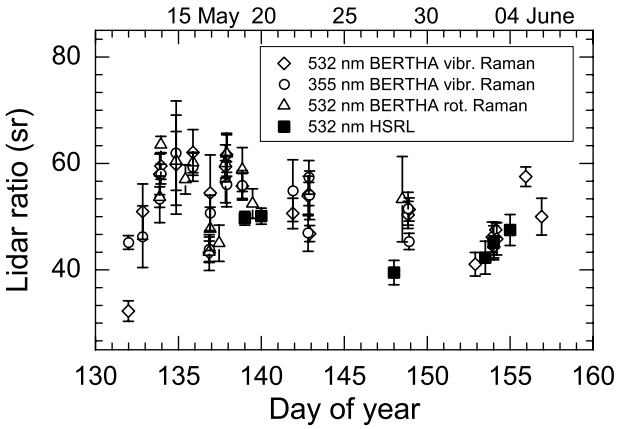

Fig. 9. Column averaged lidar ratios measured by the IFT BERTHA Raman lidar from 12 May to 6 June. The squares denote the DLR HSRL column averaged lidar ratios measured during the OZZ overpasses.

constant with height. Values average out at 0.002 km^{-1} sr^{-1} in case of the backscatter coefficient and 0.1 km^{-1} in case of the extinction coefficient. Thus, the corresponding lidar ratio profile amounts to 50 sr on average and shows a slight decrease towards the top of the layer. The aerosol depolarization ratio is almost constant with height at 30%.

In contrast to this homogeneous case Fig. 11 shows the stratification encountered on RF7. The lidar profiles were averaged close to ZAG ground station over 121 s. The backscatter profile indicates the two-layer structure of this case with values of 0.002 km^{-1} sr^{-1} within the upper dust layer above 3 km asl and 0.0045 km^{-1} sr^{-1} below. The corresponding lidar ratio profile shows values of (40 ± 5) sr within the upper layer and (48 ± 4) sr within the lower one. The depolarization ratio averages out at (30 ± 4) %. The corresponding wind direction and potential temperature profiles indicates three different layers. The bottom most from surface to 1.5 km asl is turbulent and attributed to the development of the boundary layer. The layer from 1.5 to 2.7 km asl is characterized by a defined southwesterly wind advection and separated by a slight wind shear from the top most layer reaching up to 4.2 km asl.

The three layer structure observed over QZZ on RF8 is shown in Fig. 12. The lidar signals were averaged over 97 s. The backscatter profile indicates the pronounced dust plume ranging from 2.5 to 3.5 km asl with a maximum value of 0.0049 km^{-1} sr^{-1}. The lidar ratio values are on average 42 sr within this dust plume and 50 sr within the layers below 2.5 km and above 3.5 km asl. The depolarization ratio profile is constant with height at 30% but indicates a slight notch at 3.5 km asl. The wind direction profile shows a southerly advection from 2 km up to 3.5 km asl and a westerly one above. The potential temperature is constant from 2 up to 2.5 km asl and indicates stable stratification above.

The analysis of radiosonde water vapour profiles of the respective flight missions shows no significant dependency of the lidar ratio on relative humidity.

4. Discussion

To investigate potential dependencies of the observed lidar ratio's variability on different source regions, backward

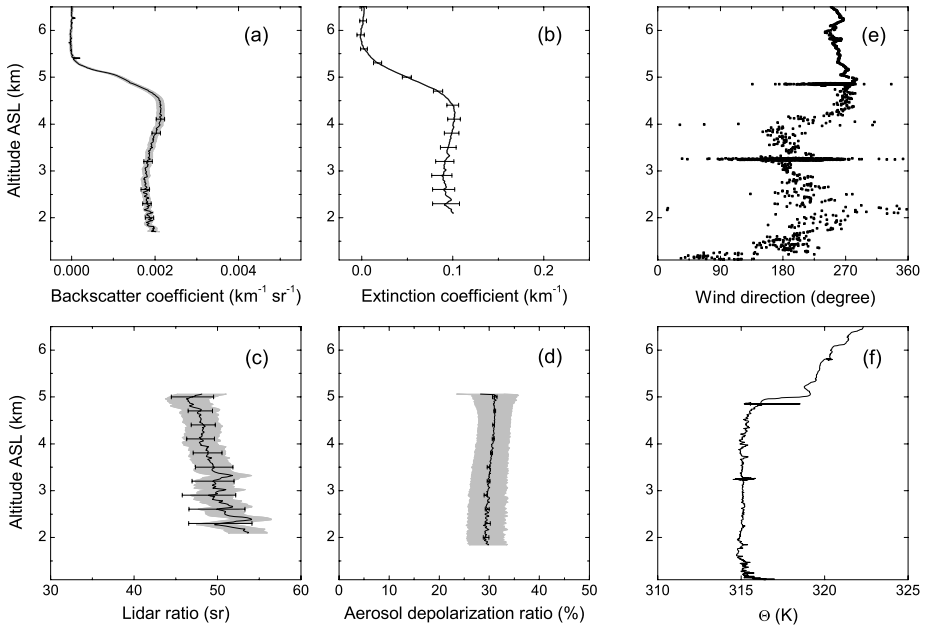

Fig. 10. Lidar profiles of the aerosol backscatter coefficient (a), extinction coefficient (b), lidar ratio (c) and aerosol depolarization ratio (d) measured on 19 May at 11:09 UTC over OZZ region. The error indicate the 3σ statistical error, the systematic error is shaded. Temporal averaging is 284 s. Falcon wind direction (e) and potential temperature (f) measurement during descent to OZZ from 11:12 to 12:12 UTC.

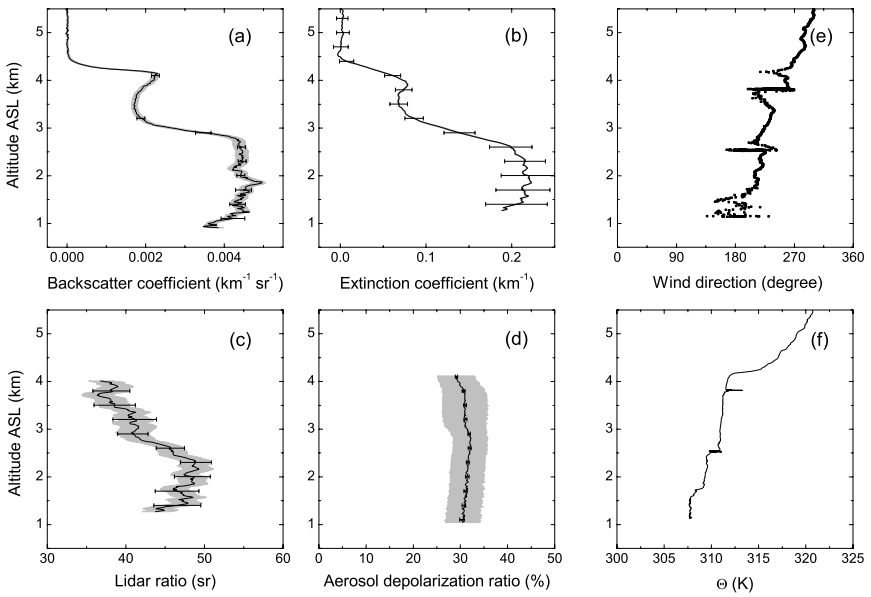

Fig. 11. Profiles of the aerosol backscatter coefficient (a), extinction coefficient (b), lidar ratio (c) and aerosol depolarization ratio (d) measured on 3 June at 07:40 UTC over ZAG region. The error indicate the 3σ statistical error, the systematic error is shaded. Temporal averaging is 121 s. Falcon wind direction (e) and potential temperature (f) measurement during descent to ZAG from 08:02–08:44 UTC.

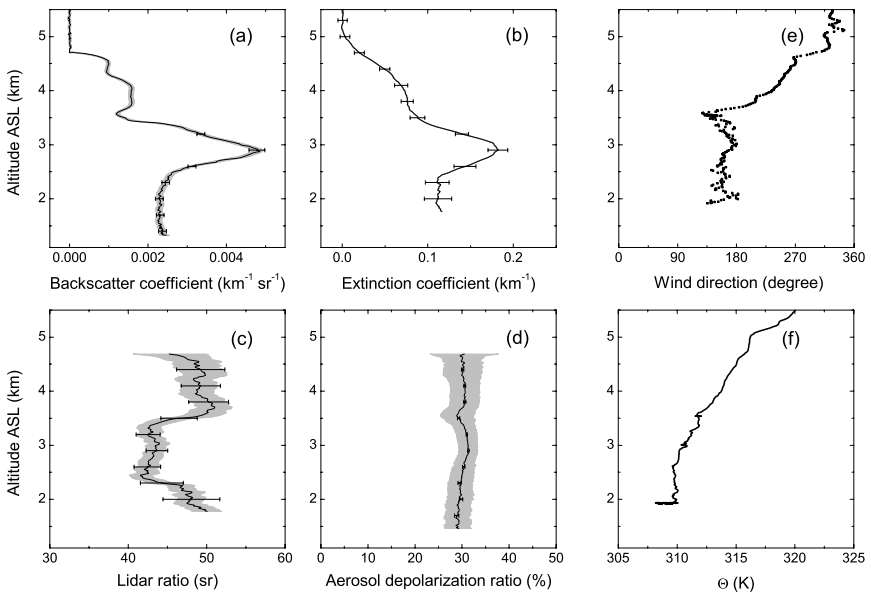

Fig. 12. Profiles of the aerosol backscatter coefficient (a), extinction coefficient (b), lidar ratio (c) and aerosol depolarization ratio (d) measured on 4 June at 09:47 UTC over OZZ region. The error indicate the 3σ statistical error, the systematic error is shaded. Temporal averaging is 97 s. Falcon wind direction (e) and potential temperature (f) measurement during ascent from OZZ from 10:31 to 10:43 UTC.

trajectories have been calculated using the LAGRANTO model (Wernli and Davis, 1997). Potential dust source regions during the SAMUM field experiment were estimated by Petzold et al. (2008) from a combined analysis of the backward trajectories, ECMWF wind fields, WMO (World Meteorological Organisation) dust storm reports and MSG (Meteosat 2nd Generation) satellite imagery. As a prerequisite for identifying a specific region as a potential dust source, the trajectories reach close to its surface with $p > 880$ hPa, the threshold of surface winds is 5–7 m s^{-1}, MSG images show dust plumes and dust events are indicated by WMO dust storm reports. A detailed study of the meteorological conditions during SAMUM and an identification of potential source regions are presented by Knippertz et al. (2008).

Figure 13 shows the backward trajectories for RF1 (panel a), RF7 (panel b), and RF8 (panel c) arriving at the times

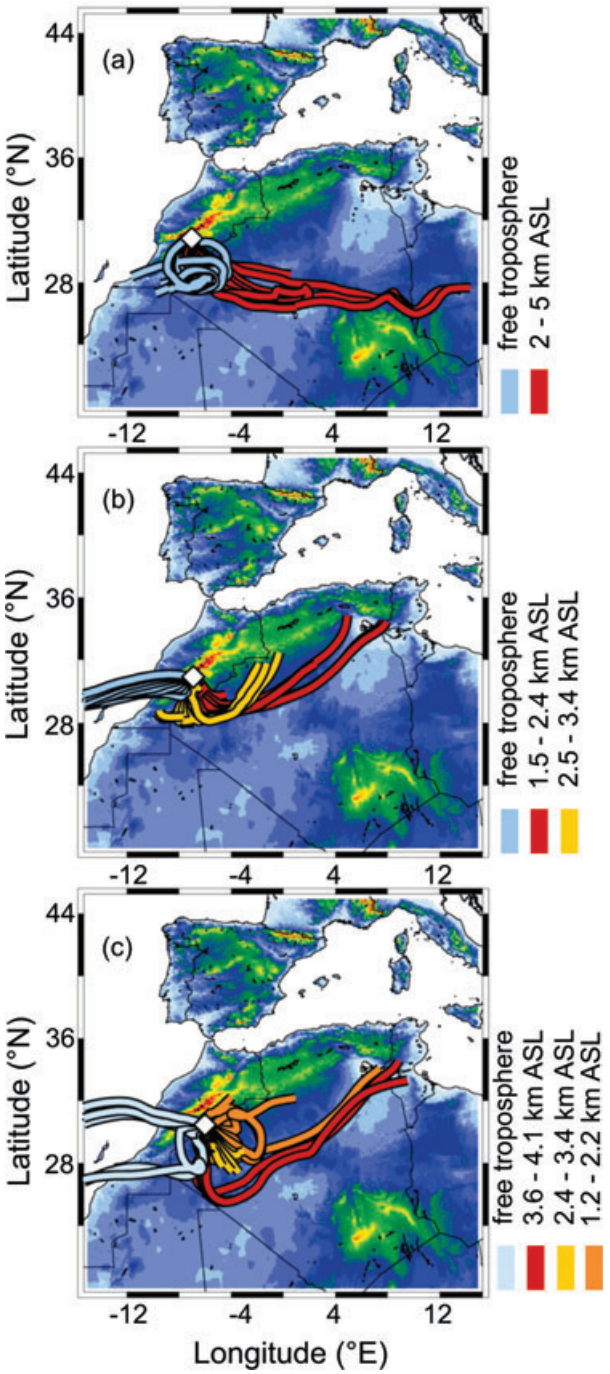

Fig. 13. Backward trajectories arriving at the times and places of the measured lidar ratio profiles on (a) RF1, (b) RF7 and (c) RF8. See text for detailed explanation.

and places the lidar ratio profiles were measured. In each case the atmospheric column from ground to 6 km asl was divided into 22 pressure levels with equal logarithmic spacing and a 100 h backward trajectory was calculated for each level. The trajectories shown in Fig. 13 run from the moment at which all the four aforementioned conditions for source region identification were met for the first time. For convenience they are grouped in color such that trajectories with the same color arrive in a specific layer of the lidar ratio profile. Trajectories arriving in the free troposphere (cyan colored) are included for the sake of completeness. As can be seen in Fig. 13a the dust layer observed on RF1 is mainly advected from central and eastern parts of Algeria and to some amount from western parts of Libia. The red trajectories arrive at pressure levels ranging from 810–571 hPa (2–5 km asl). As can be seen in Fig. 13b the two dust layers observed on RF7 originate from two different regions. The lower layer of the measured lidar ratio profile (cf. Fig. 11c) is advected from the lowlands and salt lakes in northeastern Algeria and Tunisia. The trajectories indicating the near surface dust advection are red colored and range from 850–765 hPa (1.5–2.4 km asl). The upper dust layer is seen to originate from the southern Atlas' foothills between Morocco and Algeria. The trajectories indicating the dust advection in the upper layer are yellow colored and range from 749–672 hPa (2.5–3.4 km asl). The trajectory analysis of RF8 is shown in Fig. 13c. The near surface advection ranging from 880–777 hPa (1.2–2.2 km asl), orange colored, is not well defined. Trajectories arrive from the regional southern Atlas' foothills and the salt lakes in northeastern Algeria and Tunisia. The trajectories of the middle layer 761–670 hPa (2.4–3.4 km asl), yellow colored, arrive from southwestern vicinities. The dust advection within the upper layer 655–614 hPa (3.6–4.1 km asl) is seen to originate from the lowlands and salt lakes in northeastern Algeria and Tunisia.

The backward trajectory analysis shows that layers, which can be differentiated by their lidar ratio, were advected from different regions. Moreover, the analysis consistently shows that dust advected from central Algeria as well as from the lowlands and salt lakes in northeastern Algeria and Tunisia shows lidar ratios of (50 $\pm$ 4) sr, whereas the local influence results in lower lidar ratios of (41 $\pm$ 4) sr. Thus, the observed lidar ratio's variability is mainly attributed to different source regions. The source regions, which were estimated during SAMUM are in close agreement to those found by Caquineau et al. (2001). For the case of RF7 significant variation of the in situ measured Ångström exponent of particle absorption was associated with different source regions (Petzold et al., 2008).

Compared to long-term lidar ratio observations in southern Europe our values agree well regarding the fact that all compared lidar ratio measurements were made at 355 nm. Balis et al. (2004) report an average lidar ratio of (51 $\pm$ 24) sr measured at Thessaloniki, Greece with a Raman lidar. A total of 12 cases distributed over roughly 1.5 yr were averaged. Mona et al. (2006) state an average lidar ratio of (38 $\pm$ 15) sr for Saharan dust in the absence of maritime aerosol. The measurements were made at Potenza, Italy during a three-year climatology of desert dust. Amiridis et al. (2005) give (57 $\pm$ 28) sr as the mean lidar ratio at Thessaloniki, Greece measured with a Raman lidar during a four-year study. Recently, Papayannis et al. (2008) reported mean lidar ratio values for Southern Europe of the order of

(35 ± 15) up to (58 ± 15) sr inside the dust layer. The measurements were made with Raman lidars at 351 and 355 nm during May 2000 to December 2002. The large standard deviation in each case reflects the natural variability of this quantity.

5. Conclusion

We have presented airborne HSRL measurements of pure Saharan dust during SAMUM 2006. The spatial distribution of the desert dust plumes was discussed on the basis of six Falcon flight missions. The internal structure of the dust plumes varied from homogenous to stratified. The layers extended from surface up to 4–6 km asl and usually exhibited a sharply defined boundary. Maximum AOT values of these layers measured at 532 nm during the flight missions were 0.50–0.55. Significant horizontal variability of the AOT was observed even in cases of a well mixed dust layer. This variation along the flight path was attributed to the in influence of topography in cases of well mixed layers and to layer inhomogeneities, respectively. Lidar ratio values measured by HSRL ranged from 38–50 sr. The lidar ratio profiles showed distinct stratification depending on the vertical structure of the dust layer. The unexpectedly large variability of the pure dust lidar ratios was mainly attributed to dust advection from different origins. In contrast to the lidar ratio's vertical variation, the depolarization ratio of the pure Saharan dust was $(30 \pm 4)\%$ at 532 nm during all research flights and has shown virtually no variation along the profile.

6. Acknowledgments

The present study was supported by the German Research Foundation within the Research Group SAMUM. Additionally, we received funding of the European Space Agency (ESA) under contract No. 19429/06/NL/AR. Founding of the European Fleet for Airborne Research (EUFAR) as part of the Desert Dust and Biomass Burning Aerosols over Portugal (DARPO) project is gratefully acknowledged. We would like to thank Christoph Kiemle (DLR) for his support during the field campaign in Morocco. Additionally, we would like to thank the DLR Flight Facilities for perfect collaboration during SAMUM. We wish to thank Thomas Hamburger (DLR) for calculation of the LAGRANTO trajectories. Access to the ECMWF operational forecast and analyses products was made possible by a special project of Andreas Dörnbrack (DLR). Two anonymous reviewers provided helpful suggestions and comments.

References

Amiridis, V., Balis, D. S., Kazadzis, S., Bais, A., Giannakaki, E. and co-authors. 2005. Four–year aerosol observations with a Raman lidar at Thessaloniki, Greece, in the framework of European Aerosol Research Lidar Network (EARLINET). *J. Geophys. Res.* **110**, doi:10.1029/2005JD006190.

Ansmann, A., Riebesell, M. and Weitkamp, C. 1990. Measurement of atmospheric aerosol extinction profiles with a Raman lidar. *Opt. Lett.* **14**, 746–748.

Ansmann, A., Wagner, F., Althausen, D., Müller, D., Herber, A. and co-authors. 2001. European pollution outbreaks during ACE 2: Lofted aerosol plumes observed with Raman lidar at the Portuguese coast. *J. Geophys. Res.* **106**, 20 725–20 734.

Balis, D. S., Amiridis, V., Nickovic, S., Papayannis, A. and Zerefos, C. 2004. Optical properties of Saharan dust layers as detected by a Raman lidar at Thessaloniki. *Geophys. Res. Lett.* **31**, doi:10.1029/2004GL019881.

Bösenberg, J. et al. 2003. A European aerosol research lidar network to establish an aerosol climatology. *MPI–Report* **317**, Max–Planck Inst. für Meteorologie, Hamburg, Germany.

Caquineau, S., Gaudichet, A., Gomes, L. and Legrand, M. 2002. Mineralogy of Saharan dust transported over northwestern tropical Atlantic Ocean in relation to source regions. *J. Geophys. Res.* **107**, doi: 10.1029/2000JD000247.

De Tomasi, F., Blanco, A. and Perrone M. R. 2003. Raman lidar monitoring of extinction and backscattering of African dust layers and dust characterization. *Appl. Optics* **42**, 1699–1709.

Dinter, T., von Hoyningen–Hüne, W., Kokhanovsky, A., Burrows, J., Bierwirth, E. and co-authors. 2008. Retrieval of aerosol optical thickness for desert conditions using MERIS observations during the SAMUM campaign. *Tellus* **61B**, doi: 10.1111/j.1600-0889.2008.00391.x.

Esselborn, M., Wirth, M., Fix, A., Tesche, M. and Ehret G. 2008. Airborne high spectral resolution lidar for measuring aerosol extinction and backscatter coefficients. *Appl. Optics* **47**, 346–358.

Freudenthaler, V., Esselborn, M., Wiegner, M., Heese, B., Tesche, M. and co-authors. 2008. Depolarization–ratio profiling at several wavelengths in pure Saharan dust during SAMUM. *Tellus* **61B**, doi: 10.1111/j.1600-0889.2008.00396.x.

GLOBE Task Team and others 1999. *The Global Land One–kilometer Base Elevation (GLOBE) Digital Elevation Model, Version 1.0.* (eds. D. A. Hastings, P. K. Dunbar, G. M. Elphingston, M. Bootz, H. Murakami and co-editors). National Oceanic and Atmospheric Administration, National Geophysical Data Center , 325 Broadway, Boulder, CO 80303.

Haywood, J. and Boucher O. 2000. Estimates of the direct and indirect radiative forcing due to tropospheric aerosols: a review. *Rev. Geophys.* **38**, 513–543.

Haywood, J. M., Francis, P. N., Geogdzhhayev, I., Mishchenko, M. and Frey R. 2001. Comparison of Saharan dust aerosol optical depths retrieved using aircraft mounted pyranometers and 2–channel AVHRR algorithms. *Geophys. Res. Lett.* **28**, 2393–2396.

Heintzenberg, J. 2008. The SAMUM–1 experiment over Southern Morocco: overview and introduction. *Tellus* **61B**, doi: 10.1111/j.1600-0889.2008.00403.x.

Kahn, R., Petzold, A., Wendisch, M., Bierwirth, E., Dinter, T. and co-authors. 2008. Desert dust aerosol air mass mapping in the western Sahara, using particle properties derived from space–based multi–angle imaging. *Tellus* **61B**, doi: 10.1111/j.1600-0889.2008.00398.x.

Knippertz, P., Ansmann, A., Althausen, D., Müller, D., Tesche, M. and co-authors. 2008. Dust mobilization and transport in the Northern Sahara during SAMUM 2006: a meteorological overview. *Tellus* **61B**, doi: 10.1111/j.1600-0889.2008.00380.x.

Mattis, I., Ansmann, A., Müller, D., Wandinger, U. and Althausen, D. 2002. Dual-wavelength Raman lidar observations of the extinction-to-backscatter ratio of Saharan dust. *Geophys. Res. Lett.* **29**, doi:10.1029/2002GL014721.

Mona, L., Amodeo, A., Pandolfi, M. and Pappalardo, G. 2006. Saharan dust intrusions in the Mediterranean area: three years of Raman lidar measurements. **111**, D16203, doi:10.1029/2005JD006569.

Müller, D., Mattis, I., Wandinger, U., Ansmann, A., Althausen, D. and co-authors. 2003. Saharan dust over a central European EARLINET–AERONET site: combined observations with Raman lidar and Sun photometer. *J. Geophys. Res.* **108**, doi:10.1029/2002JD002918.

Papayannis, A., Balis, D., Amiridis, V., Chourdakis, G., Tsaknakis, G. and co-authors. 2005. Measurements of Saharan dust aerosols over the Eastern Mediterranean using elastic backscatter-Raman lidar, spectrophotometric and satellite observations in the frame of the EARLINET project. *Atmos. Chem. Phys.* **5**, 2065–2079.

Papayannis, A., Amiridis, V., Mona, L., Tsaknakis, G., Balis, D. and co-authors. 2008. Systematic lidar observations of Saharan dust over Europe in the frame of EARLINET (2000-2002). *J. Geophys. Res.* **113**, D10204, doi:10.1029/2007JD009028.

Petzold, A., Rasp, K., Weinzierl, B., Esselborn, M., Hamburger, T. and co-authors. 2008. Saharan dust absorption and refractive index from aircraft–based observations during SAMUM 2006. *Tellus* **61B**, doi: 10.1111/j.1600-0889.2008.00383.x.

Penner, J. E., Andreae, M. O., Annegarn, H, Barrie, L., Feichter, J. and co-authors. 2001. Aerosols, their direct and indirect effects. In: *Climate Change 2001: The Scientific Basis. Contribution of Working Group I to the Third Assessment Report of the Intergovernmental Panel on Climate Change* (eds. J. T.. Houghton and Y. Ding). Cambridge University Press, Cambridge, UK , and New York, NY, USA, 289–348.

Piironen, P. and Eloranta, E. W. 1994. Demonstration of a high–spectral–resolution lidar based on an iodine absorption filter. *Optics Lett.* **19**, 234–236.

Powell, D. M., Reagan, J. A., Rubio, M. A., Erxleben, W. H. and Spinhirne, J. D. 2000. ACE-2 multiple angle micro-pulse lidar observations from Las Galletas, Tenerife, Canary Islands. *Tellus* **52B**, 652–661.

Sakai, T., Shibata, T., Kwon, S. A., Kim, Y. S., Tamura, K. and co-authors. 1999. Free tropospheric aerosol backscatter, depolarization ratio, and relative humidity measured with the Raman lidar at Nagoya in 1994–1997: contributions of aerosols from the Asian Continent and the Pacific Ocean. *Atmos. Environ.* **34**, 431–442.

Shimizu, H., Lee, S. A. and She, C. Y. 1983. High spectral resolution lidar system with atomic blocking filters for measuring atmospheric parameters. *Appl. Optics* **22**, 1373–1381.

Shipley, S. T., Tracy, D. H., Eloranta, E. W., Trauger, J. T., Sroga, J. T. and co-authors. 1983. High spectral resolution lidar to measure optical scattering properties of atmospheric aerosols. 1: theory and instrumentation. *Appl. Optics* **22**, 3716–3724.

Solomon, S., Qin, D., Manning, M., Chen, Z., Marquis, M. and co-editors. 2007. *The Physical Science Basis. Contribution of Working Group I to the Fourth Assessment Report of the Intergovernmental Panel on Climate Change*. Cambridge University Press, Cambridge, United Kingdom and New York, 153–180.

Tegen, I., Hollrig, P., Chin, M., Fung, I., Jacob, D. and co-authors. 1997. Contribution of different aerosol species to the global aerosol extinction optical thickness: Estimates from model results. *J. Geophys. Res.* **102**, 23 895–23 916, doi:10.1029/97JD01864.

Tesche, M., Ansmann, A., Müller, D., Althausen, D., Heese, B. and co-authors. 2008. Vertical profiling of Saharan dust with Raman lidars and airborne HSRL in southern Morocco during SAMUM. *Tellus* **61B**, doi: 10.1111/j.1600-0889.2008.00390.x.

Voss, K. J., Welton, E. J., Quinn, P. K., Johnson, J., Thompson, A. M. and co-authors. 2001. Lidar measurements during Aerosols99. *J. Geophys. Res.* **106**, 20 821–20 831.

Wagner, F., Bortoli, D., Pereira, S., Costa, M.J., Silva, A. M. and co-authors. 2008. Properties of dust aerosol particles transported to Portugal from the Sahara desert. *Tellus* **61B**, doi: 10.1111/j.1600-0889.2008.00393.x.

Weinzierl, B., Petzold, A., Esselborn, M., Wirth, M., Rasp, K. and co-authors. 2008. Airborne measurements of dust layer properties, particle size distribution and mixing state of Saharan dust during SAMUM 2006. *Tellus* **61B**, doi: 10.1111/j.1600-0889.2008.00392.x.

Welton, E. J., Voss, K. J., Gordon, H. R., Maring, H., Smirnov, A. and co-authors. 2000. Ground-based lidar measurements of aerosols during ACE-2: instrument description, results, and comparisons with other ground-based and airborne measurements. *Tellus* **52B**, 636–651.

Wernli, H. and Davis, H. C. 1997. A Lagrangian-based analysis of extratropical cyclones, I: the method and some applications. *Q. J. R. Meteorol. Soc.* **123**, 467–489.

Winker, D. M., Hunt, W. H. and McGill, M. J. 2007. Initial performance assessment of CALIOP. *Geophys. Res. Lett.* **34**, doi:10.1029/2007GL030135.